Parameter optimization of extreme ultraviolet radiation from lithium targets driven by short-wavelength solid-state lasers

Jie Lin(林杰)[1,3*], Wen-Jing Fei(费雯静)[1,3*], Yun Yuan(袁赟)[1,3†], Xiao-Nan Hu(胡小楠)[1,3], Zi-Qing Zhang(张子晴)[1,3], Qing Liu(刘庆)[1,3], Wen-Peng Wang(王文鹏)[2‡], and Wen Luo(罗文)[1,3§]

[1] *School of Nuclear Science and Technology, University of South China, Hengyang 421001, China*

[2] *State Key Laboratory of High Field Laser Physics, Shanghai Institute of Optics and Fine Mechanics, Chinese Academy of Sciences, Shanghai 201800, China*

[3] *Key Laboratory of Advanced Nuclear Energy Design and Safety, Ministry of Education, University of South China, Hengyang 421001, China*

Abstract

Short-wavelength solid-state lasers are considered promising drivers for next-generation extreme ultraviolet (EUV) lithography sources owing to their compact architecture and high electro-optical conversion efficiency. Using a one-dimensional radiation-hydrodynamic model, the EUV emission characteristics of laser-driven Li plasmas were investigated, and the dependence of the in-band conversion efficiency (CE) within a 2% bandwidth centered at 13.5 nm on laser wavelength and intensity was analyzed. The results show that the optimal laser intensity increases with decreasing wavelength, while the CE exhibits a non-monotonic dependence on wavelength. A maximum CE of 2.5% was obtained at a wavelength of 0.5 μm and an intensity of 6×10^{10} W/cm^2, accompanied by a relatively high spectral purity (SP) of 22.4%. Further analysis reveals that shorter wavelengths shift laser energy deposition toward denser plasma regions, thereby increasing the radiation efficiency. However, the resulting increase in plasma optical depth enhances radiation self-absorption and re-emission processes, leading to spectral broadening and a reduction in SP. The evolution of the CE is therefore governed by the competition between radiation enhancement and spectral broadening. To boost optimization efficiency, the enhanced Bayesian optimization framework identified the reference global optimum within 25 total objective-function evaluations in a representative run, compared with 272 simulations required for exhaustive grid scanning. Additional comparisons with available Li-target experiments show good agreement in the CE–intensity trends and major EUV spectral features. These results provide physical insight into short-wavelength laser-driven Li-plasma EUV emission and demonstrate the potential of Bayesian optimization for efficient parameter optimization of laser-driven EUV sources.

Keywords: radiation hydrodynamics, EUV, laser-produced plasma, Bayesian optimization

* These authors contributed equally to this work.

†Corresponding author. E-mail: yuanyun_usc@qq.com

‡Corresponding author. E-mail: wangwenpeng@siom.ac.cn

§Corresponding author. E-mail: wenluo-ok@163.com

PACS: 52.25.Os, 52.50.Jm, 42.55.Vc, 02.60.Pn

1. Introduction

Extreme ultraviolet (EUV) lithography has become a critical core technology for advanced semiconductor manufacturing, providing essential support for the continuous development of highly integrated and small-scale devices [1–4]. Laser-produced plasma (LPP) is currently the mainstream EUV light source scheme [5–12], the fundamental principle of which is to use high-power laser irradiation on a target to form a high-temperature, high-density plasma that radiates EUV light near 13.5 nm [13,14]. Currently, improving the conversion efficiency (CE) of EUV radiation within a 2% bandwidth centered at 13.5 nm remains one of the core issues in EUV source research [15]. The CE is jointly determined by the spectral purity (SP) and radiation efficiency (η_{rad}), following the relation $CE = SP \times \eta_{\mathrm{rad}}$. Here, SP is defined as the fraction of the total emitted radiation energy contained within 13.365–13.635 nm, while η_{rad} denotes the fraction of incident laser energy converted into total radiation energy. CE therefore represents the fraction of incident laser energy converted into radiation within the same in-band wavelength range [16,17]. Enhanced out-of-band radiation leads to a reduction in SP, which not only decreases the effective in-band EUV output but also increases the thermal load on optical components. Therefore, maintaining a high SP is equally important while pursuing a high CE.

In recent years, short-wavelength solid-state lasers have gained increasing attention as an alternative to the traditional 10.6 μm carbon dioxide (CO_2) laser [18,19]. Compared to CO_2 lasers, solid-state lasers have advantages such as a smaller size, higher electro-optical conversion efficiency, and easier integration, which are expected to further enhance the high-volume manufacturing capability and economic viability of EUV lithography systems [20,21]. Currently, tin (Sn) remains the core target material for mainstream EUV lithography sources, and extensive research has been conducted on its laser parameter optimization and EUV radiation enhancement. In early studies, Shimada et al. [22] used multiple laser beams to irradiate Sn-coated spherical plastic targets and obtained a CE of 3.0%. Subsequently, Tao et al. [23] used an Nd:YAG laser to drive Sn plasma and achieved a relatively stable in-band radiation output. Further research has shown that by optimizing the laser wavelength, using pre-pulses, and tailoring beam profiles, CE can be increased to 4.1%–7.1% [24–29]. However, under short-wavelength laser-driven conditions, the strong opacity effect of Sn plasma can easily cause spectral broadening and enhanced out-of-band radiation, thereby limiting the further improvement of SP and exacerbating optical element contamination and damage [30,31]. In addition to Sn, studies on gadolinium (Gd) as a candidate target material for Beyond EUV lithography sources have also revealed similar patterns [32]. Dou et al. [33] systematically investigated the 6.7 nm emission characteristics and ion debris distribution of Gd planar targets irradiated by a 1064 nm laser, while Xie et al. [34] achieved spectral narrowing and enhanced emission intensity using dual-pulse laser irradiation of Gd targets. However, owing to the complex electronic configurations of Gd atoms, significant spectral line overlap and out-of-band radiation remain in the emission spectrum, thereby limiting further improvement of the SP. In contrast, lithium (Li) exhibits great research potential due to

its relatively simple atomic structure and unique radiation characteristics. EUV radiation generated from Li plasma is mainly composed of discrete line spectra, which are less affected by spectral broadening [35,36]. At the same time, its out-of-band radiation heat load is lower, and the energy of produced debris is less, which is beneficial for prolonging the lifetime of optical elements [37]. Explorations of EUV radiation from Li plasmas have been carried out. For instance, Coons et al. [38] analyzed the plasma characteristics by irradiating pure Li planar targets with a 1 μm Nd:YAG laser pulse. Higashiguchi et al. [39] used 532 nm and 1064 nm dual-pulse lasers to drive Li targets and obtained a CE of approximately 2% in 20–50 ns pulses. However, self-consistent simulation studies on the evolution of the CE and SP, as well as the underlying physical mechanisms in short-wavelength laser-driven Li target EUV emission, remain relatively limited.

By varying the laser wavelength and laser intensity, this work investigates the EUV emission characteristics of Li plasmas and the coupling relationships among the CE, SP, and η_{rad}. The results show that the highest in-band CE within a 2% bandwidth centered at 13.5 nm, reaching 2.5%, is achieved at a laser wavelength of 0.5 μm and a laser intensity of 6×10^{10} W/cm^2, while maintaining a relatively high SP of 22.4%. The results indicate that shorter-wavelength lasers enhance local energy deposition in high-density plasma regions and thereby improve the radiation efficiency. However, they also increase the plasma optical depth, strengthening radiation self-absorption and re-emission processes, which lead to spectral broadening. The competition between radiation enhancement and spectral broadening ultimately governs the evolution of the CE. Furthermore, to improve parameter-optimization efficiency, an improved Bayesian optimization strategy was developed by combining Latin hypercube sampling with a dynamically adjusted acquisition function, enabling rapid localization of the global optimal parameter region with relatively few iterations. These findings provide theoretical insight into the physical processes of short-wavelength laser-driven EUV emission and its parameter optimization.

2. Simulation model

The simulations are performed using the MULTI-1D code [40–42], which self-consistently describes the interaction between laser pulses and high-density plasmas by incorporating the key physical processes involved in laser–plasma coupling, including hydrodynamic evolution, laser deposition, electron energy transport and multigroup radiation transport. Within this framework, laser energy absorption is modeled using the inverse bremsstrahlung absorption mechanism [43], while the electron collision frequency is calculated using the Drude–Sommerfeld model [44], which determines the electron thermal conductivity. The reduced form of the radiation transport equation is:

$$\frac{dS}{dx} = 4\pi\eta - \chi cU, \tag{1}$$

where S is the radiation energy flux, U is the radiation energy density, η is the emissivity coefficient, and χ is the absorption coefficient. The full frequency range $0 \sim \infty$ is discretized into N_G groups, with the frequency interval of the k-th group defined as $\nu_{k-1} < \nu < \nu_k$ (where $\nu_0 = 0$ and $\nu_{N_G} = \infty$). The transport

equations for the k-th group are then formulated as:

$$\frac{dS_k}{dx} = c\chi_k^P \left(\varepsilon_k U_k^P - U_k\right), \tag{2}$$

$$S_k = -\frac{1}{4}\frac{c}{\chi_k^R}\frac{dU_k}{dx}, \tag{3}$$

where U_k and S_k are the group-integrated radiation energy density and flux, respectively. In the above equations, $U_k^P = \frac{4\pi}{c}\int_{\nu_{k-1}}^{\nu_k} I^P(\nu,T)d\nu$ is the Planck energy density, χ_k^P is the Planck mean absorption coefficient, χ_k^R is the Rosseland mean absorption coefficient and ε_k is the normalized group-integrated emissivity coefficient. These group-averaged quantities are defined as:

$$\chi_k^P = \frac{\int_{\nu_{k-1}}^{\nu_k} \chi I^P d\nu}{\int_{\nu_{k-1}}^{\nu_k} I^P d\nu}, \tag{4}$$

$$\chi_k^R = \frac{\int_{\nu_{k-1}}^{\nu_k} \frac{\partial I^P}{\partial T} d\nu}{\int_{\nu_{k-1}}^{\nu_k} \frac{1}{\chi}\frac{\partial I^P}{\partial T} d\nu}, \tag{5}$$

$$\varepsilon_k = \frac{\int_{\nu_{k-1}}^{\nu_k} \eta d\nu}{\int_{\nu_{k-1}}^{\nu_k} \chi I^P d\nu}, \tag{6}$$

where $I^P = \frac{2h\nu^3}{c^2\left(e^{h\nu/kT}-1\right)}$ is the Planckian intensity of radiation at temperature T. In the present calculations, the photon-energy range from 1 to 400 eV is discretized into 136 groups. The Planck and Rosseland mean opacities required for the radiation-transport calculations are generated using the non-LTE atomic physics code FLYCHK [45] by solving collisional-radiative rate equations that account for radiative and collisional processes, autoionization, and electron capture. The resulting opacity data are then tabulated and incorporated into MULTI-1D, providing the necessary atomic-physics inputs for the multigroup radiation-transport calculations and enabling a self-consistent coupling between the plasma evolution and radiation transport. The equation of state (EOS) for the Li target is calculated based on the Quotidian equation of state (QEOS) model proposed by More [46], which includes the ideal gas model, Debye-Einstein model, and Thomas-Fermi model.

The simulation process of laser irradiation on a Li target is shown in Fig. 1, where the Li target is a planar target with a thickness of 25 μm and an initial density set to 0.534 g/cm^3. The laser pulse width is uniformly set to 10 ns, with a square waveform. The laser wavelengths are taken as 2 μm, 1 μm, 0.5 μm, 0.35 μm, 0.266 μm, 0.212 μm, 0.151 μm, and 0.1 μm. Among them, the 2 μm and 1 μm lasers are typical Tm/Ho-based and Nd/Yb-based solid-state lasers, respectively, while the 0.5 μm to 0.212 μm lasers are the second to fifth harmonic frequencies of the 1 μm laser. Although the realization of fifth- and higher-order harmonic lasers remains technically challenging under current experimental conditions, these higher harmonics are introduced here as theoretical parameters. The purpose is to investigate the evolution of laser–plasma interaction and radiation characteristics in the short-wavelength limit, thereby revealing the scaling behavior and underlying physical mechanisms of the relevant processes. It should be noted that the present one-dimensional planar model provides an idealized description of the laser-driven plasma evolution. The multidimensional expansion induced by the finite focal spot may therefore affect the calculated CE. A fully quantitative assessment, however, would require self-consistent two- or

three-dimensional radiation-hydrodynamic simulations. The applicability of this approximation and the possible influence of multidimensional expansion are further discussed in Sec. 4.1.

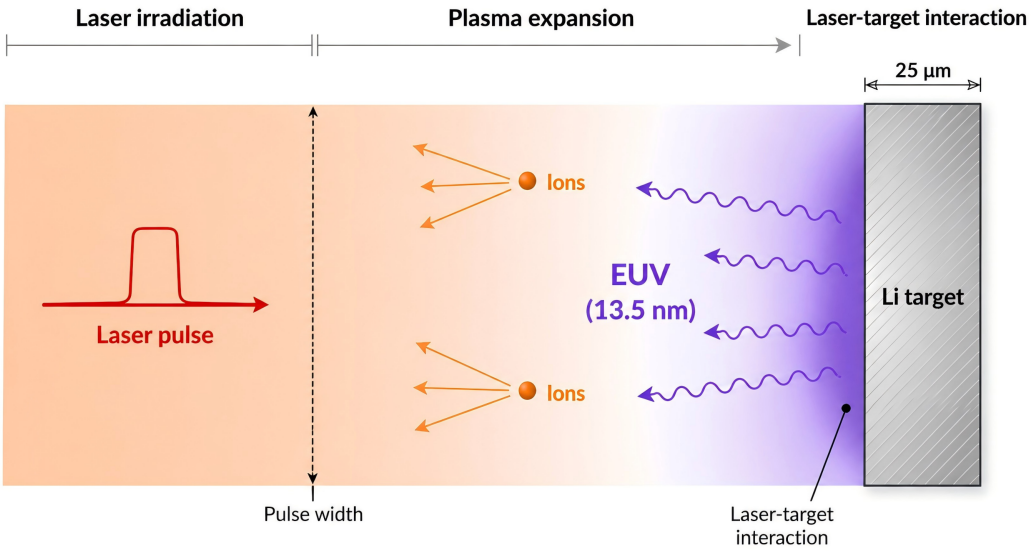


Fig. 1. Simulation process of laser irradiation on solid Li target.

3. Simulation and Bayesian Optimization results

3.1. Simulation results

Fig. 2(a) shows the evolution of EUV CE with laser wavelength ($\lambda_L = 0.1$–2 μm) and laser intensity ($I_L = 2\times10^9$–8×10^{12} W/cm^2). When the wavelength is fixed, the CE shows a trend of first increasing and then decreasing with the laser intensity. As the wavelength decreases, the optimal laser intensity ($I_{L,\mathrm{peak}}$) increases accordingly. The optimal CE of 2.5% is obtained when $\lambda_L = 0.5$ μm and $I_L = 6\times10^{10}$ W/cm^2. This result is in good agreement with the CE variation law and optimal laser parameters reported in experiments by Nagano and Hansson et al. [37,47], where the best CE was also obtained at a wavelength of 0.5 μm. Based on the above laws, a quantitative scaling relationship between the optimal laser intensity and wavelength can be established:

$$I_{L,\mathrm{peak}} \sim \frac{1.7\times10^{10}}{\lambda_L^{1.9}}(\mathrm{W/cm^2}), \tag{7}$$

This relationship originates from the regulation of the energy deposition position by the laser critical density. For a laser with wavelength λ_L, the critical density formula is $n_c(\mathrm{cm^{-3}}) = 1.1\times10^{21}/\lambda_L^2(\mu\mathrm{m})$ [48]. Therefore, a shorter wavelength corresponds to a higher critical density, allowing the laser to deposit energy in a higher-density region closer to the target surface, thereby improving the energy coupling efficiency. However, it is also necessary to correspondingly increase the laser intensity to bring the electron temperature into the optimal range for EUV radiation. The above mechanism constitutes the physical basis for understanding the differences in energy deposition and radiation characteristics under different wavelength conditions.

To further elucidate the wavelength dependence of CE, four representative wavelengths (0.1 μm, 0.151 μm, 0.5 μm, and 1 μm) are selected from the eight wavelengths, with corresponding $I_{L,\mathrm{peak}}$ values of 1×10^{12} W/cm^2, 6×10^{11} W/cm^2, 6×10^{10} W/cm^2, and 2×10^{10} W/cm^2, respectively, indicated by the black dashed circles in Fig. 2(a). Fig. 2(b) presents the dependence of CE, SP, and η_{rad} on laser wavelength. The results indicate that as the wavelength increases, η_{rad} gradually decreases: the values under 0.1 μm, 0.151 μm, 0.5 μm, and 1 μm conditions are 20.5%, 18.2%, 11.2%, and 6.9%, respectively. In contrast, SP shows a monotonically increasing trend with increasing wavelength, with corresponding values of 6.4%, 10.3%, 22.4%, and 30.2%. The interplay of these two mechanisms results in a non-monotonic change in CE with wavelength, which first increases and then decreases, showing 1.3% (0.1 μm), 1.9% (0.151 μm), 2.5% (0.5 μm), and 2.1% (1 μm) at the four wavelengths.

The energy conversion relationship from laser to plasma energy is shown in Fig. 2(c). The absorbed laser energy is converted into plasma energy, which consists of three parts [49]:

$$E_{\mathrm{abs}} = E_{\mathrm{int}} + E_{\mathrm{kin}} + E_{\mathrm{rad}}, \tag{8}$$

where E_{abs}, E_{int}, E_{kin}, and E_{rad} represent the absorbed laser energy, the plasma internal energy, the plasma kinetic energy, and the plasma radiation energy, respectively. $E_{\mathrm{abs}} = \alpha E_l$, where E_l is the incident laser energy and α is the laser absorption coefficient. By normalizing E_L, E_{abs}, E_{int}, E_{kin}, and E_{rad} to the total incident laser energy, their respective energy fractions can be obtained and expressed as η_l, η_{abs}, η_{int}, η_{kin}, and η_{rad}. The pulse-integrated laser absorption efficiencies for the four representative wavelengths of 0.1, 0.151, 0.5, and 1.0 µm are 99.98%, 99.76%, 98.96%, and 97.78%, respectively. The wavelength dependence is mainly reflected in the early-time absorption dynamics, while strong overall laser absorption is maintained throughout the investigated cases. The overall energy balance was also examined, with the energy-conservation error remaining on the order of 10^{-3}% and the maximum absolute error below 5×10^{-3}%, confirming good energy conservation throughout the simulations. During the laser irradiation stage, the absorbed laser energy is continuously deposited in the interaction region, leading to a steady increase in E_{int}. After the laser pulse ends, the absence of further external energy input causes E_{int} to gradually decrease. Meanwhile, the high-temperature and high-pressure plasma converts E_{int} into E_{kin} through hydrodynamic expansion and into E_{rad} through radiative cooling, resulting in the continuous growth of both quantities throughout the plasma evolution. Further analysis of the absorbed energy partition reveals that, with increasing laser wavelength, E_{rad} gradually decreases while E_{int} correspondingly increases. Specifically, η_{rad} decreases from 20.5% to 6.9%, whereas η_{int} increases from 34.7% to 47.4%, indicating a significant redistribution of the absorbed laser energy between radiation and internal energy channels. In contrast, the variation in E_{kin} remains within approximately 3% across different wavelengths. Therefore, the wavelength-dependent energy conversion behavior is primarily governed by the competition between E_{rad} and E_{int}. The underlying physical mechanisms responsible for the evolution of the radiation energy will be further discussed in conjunction with the radiation emission characteristics of laser-driven plasmas.

Fig. 2(d) presents the EUV emission spectra of Li plasmas driven by lasers with four different wave-

lengths. All spectra exhibit five major characteristic peaks corresponding to resonant transitions of Li ions in different charge states: the $1s^2$–$1s2p$ resonance transition of Li^+ at 19.9 nm, the $1s^2$–$1s3p$ resonance transition of Li^+ at 17.8 nm, the 1s–2p resonance transition of Li^{2+} at 13.5 nm, the 1s–3p resonance transition of Li^{2+} at 11.39 nm, and the 1s–4p resonance transition of Li^{2+} at 10.8 nm. Among them, the 13.5 nm emission peak associated with the Li^{2+} 1s–2p resonance transition is the most intense and lies within a 2% bandwidth centered at 13.5 nm, making it the dominant contributor to the in-band EUV emission [50]. The spectral characteristics exhibit pronounced wavelength dependence. At 0.1 μm, the highest laser intensity produces a higher plasma temperature, resulting in significant spectral broadening. At 0.151 μm, the degree of spectral broadening is reduced. In contrast, under the 0.5 μm and 1 μm conditions, the main EUV peak at 13.5 nm becomes dominant, while the out-of-band radiation is substantially suppressed. These spectral variations directly affect the evolution of the SP, whose underlying mechanisms will be further analyzed in conjunction with radiation self-absorption and re-emission processes in the EUV-emitting plasma.

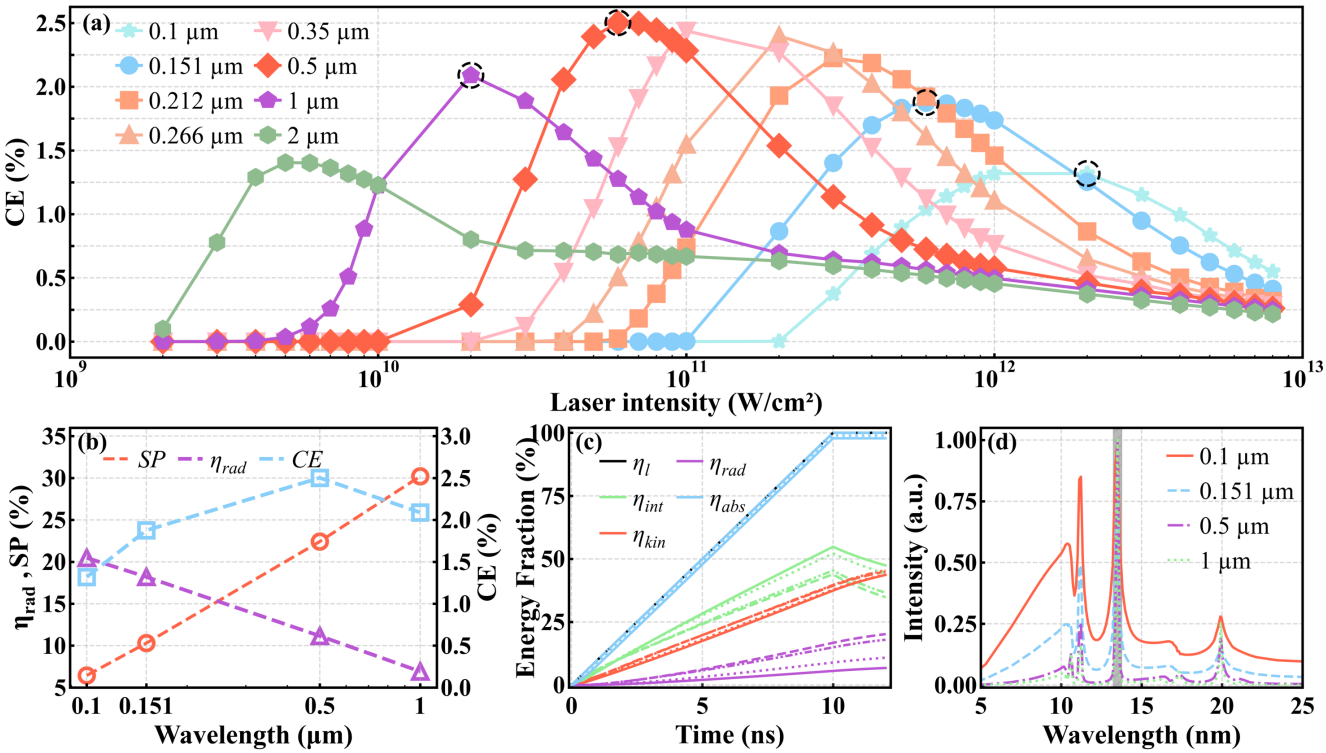


Fig. 2. The effect of laser parameters on the radiation characteristics of Li plasma. (a) EUV CE as a function of laser intensity and wavelength. (b) The relationships of SP, $\eta_{\rm rad}$, and CE with laser wavelength. (c) The temporal evolution of the energy fractions of incident laser energy η_L, absorbed laser energy $\eta_{\rm abs}$, plasma radiation energy $\eta_{\rm rad}$, plasma internal energy $\eta_{\rm int}$, and plasma kinetic energy $\eta_{\rm kin}$, corresponding respectively to incident conditions of $\lambda_L = 1$ μm (solid line), $\lambda_L = 0.5$ μm (dotted line), $\lambda_L = 0.151$ μm (dash-dot line), and $\lambda_L = 0.1$ μm (dashed line). (d) Normalized spectra at different laser wavelengths. The shaded area represents the in-band EUV radiation region at 13.5 nm with a 2% bandwidth.

To further clarify the physical mechanism underlying the influence of laser wavelength on EUV CE, Fig. 3(a)–(l) show the spatiotemporal evolution results of the average ionization degree $\bar{Z}$, electron temperature $T_{\rm e}$, normalized laser energy deposition density $L_{\rm d}$, radiative power density $\partial S/\partial x$, and mass density ρ of Li plasma under four wavelengths. When high-intensity laser irradiates the surface of a lithium target,

the laser energy is first deposited into the plasma near the critical density through inverse bremsstrahlung absorption, rapidly heating the electrons and triggering the ionization process, forming a high-temperature plasma. As the electron temperature rises, lithium atoms are ionized stepwise to Li^+, Li^{2+}, and Li^{3+} ion states, and EUV photons are generated through electron impact excitation and recombination radiation. In this process, laser heating establishes a high-temperature, high-pressure region on the target surface, and the strong pressure gradient drives material ablation, producing continuous plasma ejection, whose recoil pressure causes the Li target to move in the direction of the laser incidence [51]. For low-Z targets, the mass ablation rate satisfies $\dot{m} \propto I^{1/3}\lambda^{-4/3}$ [52], indicating that as the laser wavelength decreases, the ablation process is significantly enhanced. The numerical results are consistent with the theoretical trend. As shown in Fig. 3, at $t = 8$ ns, the 0.1 μm laser exhibits the strongest ablation driving capability, capable of propelling the target surface to a position of approximately 200 μm. In contrast, the propelling effects of the 0.151 μm and 0.5 μm lasers are significantly weaker, propelling the target surface to approximately 110 μm and 20 μm, respectively, whereas almost no obvious macroscopic displacement emerges on the target surface under the 1 μm laser. Therefore, as the laser wavelength decreases, E_{abs} is more efficiently converted into E_{kin}.

As the laser wavelength decreases, the corresponding critical density n_c increases significantly, shifting the laser energy deposition region toward a denser plasma and extending the localized deposition scale length of L_{d}. Consequently, the width of the EUV emission region L (defined as the full width at half maximum (FWHM) of $\partial S/\partial x$, as indicated by the shaded region in Fig. 3), becomes substantially larger for short-wavelength lasers. At $t = 5$ ns, the corresponding values of L for 0.1 μm, 0.151 μm, 0.5 μm, and 1 μm are 22.8 μm, 18.2 μm, 11.1 μm, and 1.3 μm, respectively. Moreover, L continues to broaden throughout the laser pulse duration. The enlarged emission region indicates that a larger volume of high-temperature plasma participates in EUV generation, enabling a greater fraction of E_{int} to be converted into E_{rad} and thereby increasing η_{rad}. However, the optical depth τ of the EUV-emitting plasma can be approximately characterized by $\tau \propto \rho L$ [53]. At $t = 5$ ns, the corresponding values of ρL for the 0.1 μm, 0.151 μm, 0.5 μm, and 1 μm cases are 1.14×10^{-4} g/cm^2, 0.88×10^{-4} g/cm^2, 0.41×10^{-4} g/cm^2, and 0.16×10^{-4} g/cm^2, respectively, indicating a substantial increase in τ at shorter wavelengths. As the plasma evolves, the continuous broadening of the emission region further increases ρL , leading to a progressive enhancement of τ during laser irradiation. The larger τ increases the probability of photon–plasma interactions, causing the emitted EUV radiation to undergo stronger self-absorption and repeated re-emission during transport through the plasma [54]. These processes redistribute radiation energy in both physical and frequency space, resulting in spectral broadening and causing the emitted radiation to progressively deviate from its original characteristic line distribution [55]. Consequently, the fraction of radiation within a 2% bandwidth centered at 13.5 nm decreases, leading to a reduction in SP. Therefore, although shorter wavelengths improve radiation generation by enhancing local energy deposition, the accompanying increase in τ intensifies radiation trapping and spectral broadening. The competition between these two effects ultimately governs the evolution of the CE.

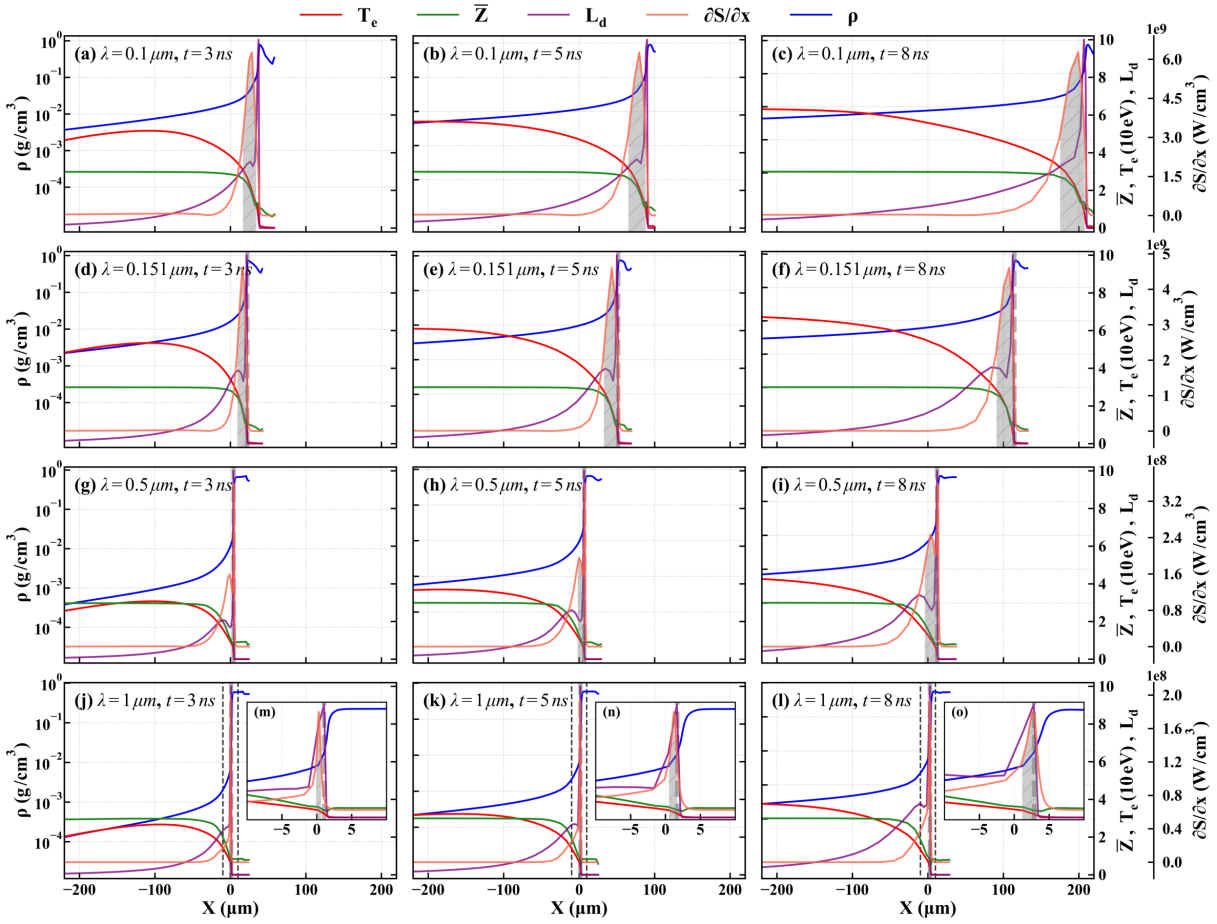


Fig. 3. Spatiotemporal evolution of EUV radiation. (a)–(l) present the spatial distributions of the average ionization $\bar{Z}$, electron temperature T_e, normalized laser energy deposition density L_d, radiative power density $\partial S/\partial x$, and mass density ρ of Li plasmas generated by four laser wavelengths at t = 3 ns, 5 ns, and 8 ns, where the thick dashed line marks the critical density surface. The shaded regions indicate the full width at half maximum (FWHM) of $\partial S/\partial x$. (m)–(o) provide magnified views of the region $x \in [-10, 10]$ μm (bounded by thin dashed lines) for the 1.0 μm case.

3.2. Bayesian optimization results

From the above analysis, it is evident that achieving a high EUV CE requires a favorable combination of laser wavelength, laser intensity, and other relevant parameters [56]. To date, CE optimization has mainly relied on parameter-scanning approaches [57]. Although effective in low-dimensional parameter spaces, the computational cost of such methods increases rapidly with the number of optimization variables, making an exhaustive search for the global optimum increasingly impractical [58]. In recent years, machine learning (ML) techniques have emerged as powerful tools for optimizing complex nonlinear systems and have been successfully applied to various laser–plasma problems [59–62]. However, the application of ML methods to EUV source optimization remains largely unexplored. Motivated by this need, the present work introduces Bayesian optimization (BO), a data-efficient approach particularly well suited for expensive black-box optimization problems [63]. The objective is to efficiently identify the optimal parameter region for maximizing CE and to establish a practical framework for data-efficient laser-plasma parameter optimization.

The present BO problem is formulated as a finite discrete search. The laser wavelength is selected

from $\lambda_L = \{0.1, 0.151, 0.212, 0.266, 0.35, 0.5, 1, 2\}\,\mu$m, and the laser intensity is selected from 34 predefined values between 2×10^9 W/cm^2 and 8×10^{12} W/cm^2. The search space therefore contains $8 \times 34 = 272$ admissible parameter combinations. At each BO iteration, the acquisition function value is evaluated for all remaining admissible candidates, and the candidate with the largest acquisition value is selected for the next MULTI-1D simulation. Each selected BO candidate corresponds to a new and independent MULTI-1D radiation-hydrodynamic simulation. The previously calculated 272-point CE dataset is not used for interpolation or objective-function lookup; this exhaustive scan serves only as an independent reference for the global optimum. No wavelength or intensity outside the predefined set is evaluated. As shown in Fig. 4(a)–(b), BO based on Gaussian process regression (GPR) was first applied to optimize the laser wavelength and intensity. After 49 iterations, the optimization converged to a local optimum at $\lambda_L = 0.35\,\mu$m and $I_L = 1\times10^{11}$ W/cm^2, yielding a CE of 2.4%, while failing to identify the global optimum. The sampling trajectory exhibits pronounced oscillations throughout the optimization process, indicating that the search remained trapped between exploration and exploitation without stable convergence to the globally optimal region. These results suggest that the conventional BO framework is insufficient for efficiently exploring the present parameter space.

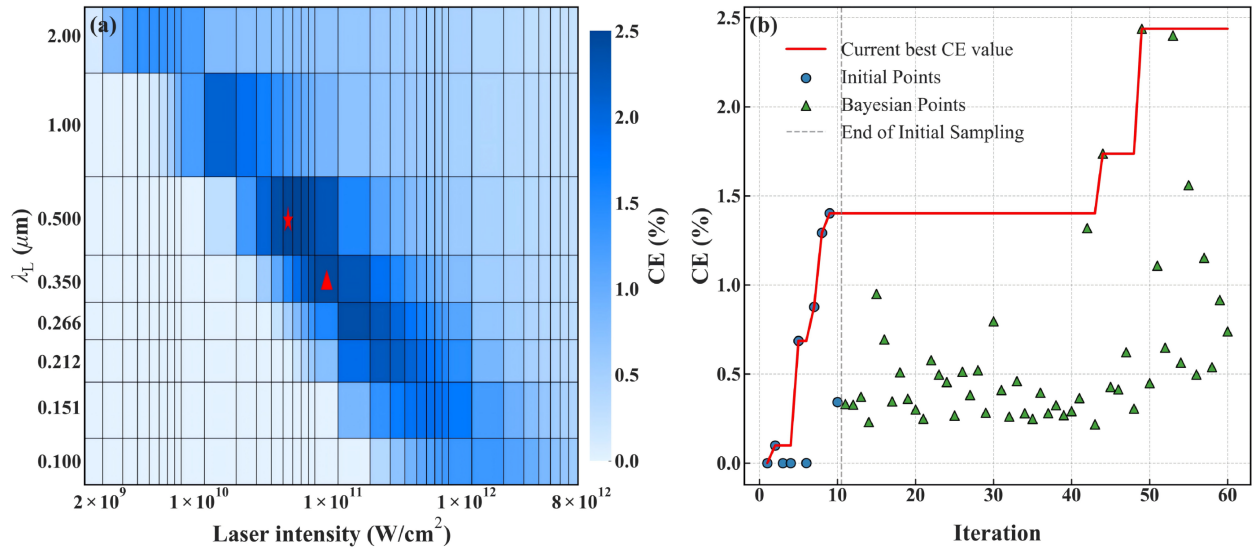


Fig. 4. Performance of the conventional Bayesian optimization framework. (a) Distribution of EUV CE in the two-dimensional parameter space of I_L and λ_L. The red star denotes the global optimum, while the red triangle marks the local optimum obtained during optimization. (b) Evolution of CE as a function of iteration number. Blue circles correspond to initial sampling points, green triangles represent sampling points selected by Bayesian optimization. The solid red line shows the best-so-far CE and the dashed gray line indicates the end of the initial sampling stage.

To improve the optimization efficiency, an enhanced BO framework was developed by combining Latin hypercube sampling (LHS) [64], a dynamically decaying upper confidence bound (UCB) acquisition function, and a random forest (RF) surrogate model. LHS was employed to improve the uniformity of the initial sampling distribution, while the dynamically adjusted UCB strategy enabled a gradual transition from global exploration to local exploitation. Meanwhile, the RF model was adopted to provide a robust representation of the nonlinear response surface under the present limited-sample conditions [65,66]. The RF surrogate contains 200 regression trees, with a maximum depth of 12 and a minimum of two samples required for an internal-node split. The mean and standard deviation of the individual-tree predictions

are used as the predictive mean $\mu(x)$ and the ensemble-based uncertainty estimate $\sigma(x)$, respectively. The UCB acquisition function is defined as

$$\mathrm{UCB}(x) = \mu(x) + \kappa_i \sigma(x), \tag{9}$$

where the exploration coefficient κ_i decreases exponentially from $\kappa_0 = 4.2$ to $\kappa_f = 0.1$,

$$\kappa_i = \kappa_0 \exp(-\beta i), \qquad \beta = \frac{\ln(\kappa_0/\kappa_f)}{N_{\mathrm{BO}} - 1}, \qquad i = 0, 1, \ldots, N_{\mathrm{BO}} - 1. \tag{10}$$

where $N_{\mathrm{BO}} = 45$ denotes the number of BO-guided evaluations following the five initial LHS samples.

The optimization results obtained using the improved BO framework are shown in Fig. 5. The CE, λ_L, and I_L all converge stably toward their optimal values, demonstrating a substantial improvement over the conventional BO approach. The globally optimal solution, corresponding to $CE_{\max} = 2.5\%$, $\lambda_L = 0.5$ μm, and $I_L = 6 \times 10^{10}$ W/cm^2, was successfully identified after only 25 total objective-function evaluations. This result is fully consistent with the optimum obtained from exhaustive grid-search calculations while reducing the computational cost by approximately one order of magnitude.

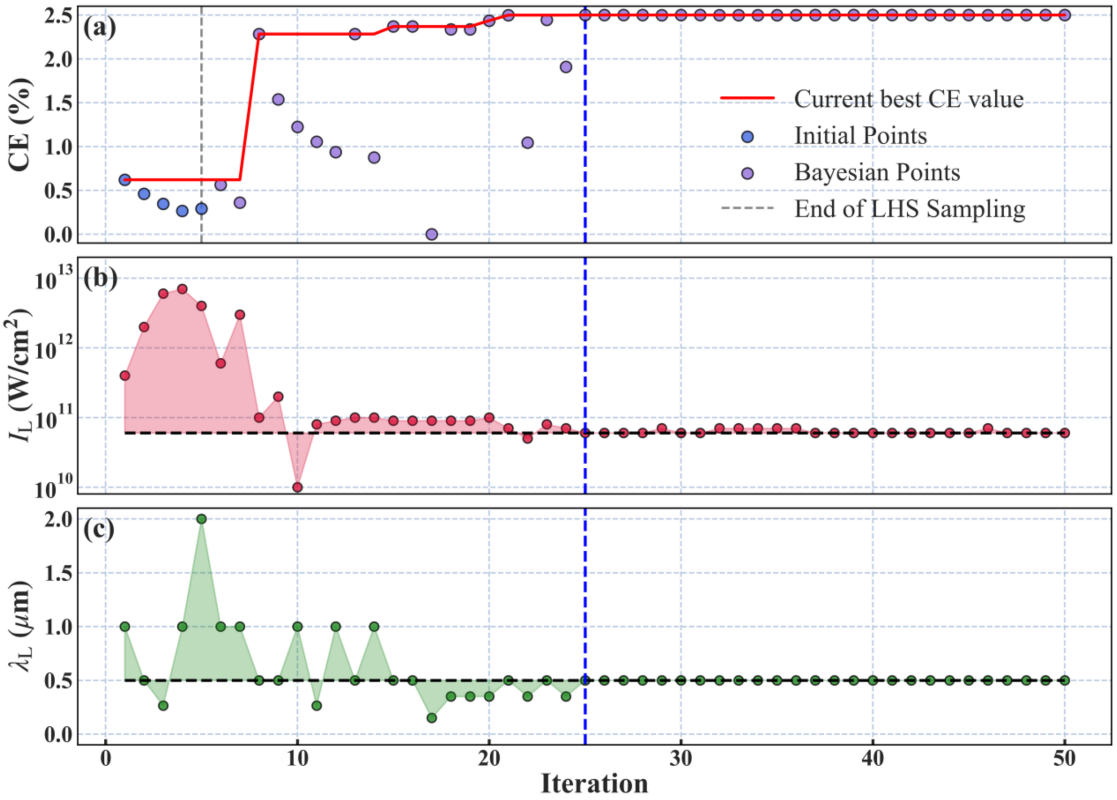


Fig. 5. Results of the improved Bayesian optimization framework. (a) Evolution of EUV CE as a function of the number of iterations. Blue circles represent initial sampling points, purple circles denote Bayesian sampling points, and the solid red line corresponds to the best-so-far CE value. The gray dashed line represents the end of initial LHS sampling. (b)–(c) Evolution of the optimized λ_L and I_L, respectively. Symbols and shaded regions denote the predicted values and associated uncertainties, while horizontal dashed lines indicate the final optimal parameters. The blue vertical dashed line marks the position where the global optimum is first identified.

4. Discussion

This section discusses the main limitations, uncertainties, and methodological choices of the present framework. A quantitative experimental benchmark of the radiation-hydrodynamic simulations is provided in Appendix A.

4.1. Applicability and limitations of the one-dimensional planar approximation

The present MULTI-1D calculations employ a one-dimensional planar geometry and therefore explicitly describe only the target-normal plasma evolution. The applicability of this approximation depends on the relative magnitudes of the transverse laser-spot size and the relevant longitudinal target and plasma scales. When the transverse laser-spot size is sufficiently large compared with the target thickness, a planar model can reasonably describe the dynamics of the dense target region, whereas lateral heat transport and plasma-flow divergence become increasingly important as the longitudinal plasma expansion approaches the transverse focal-spot scale [67]. We therefore first examine the consistency of the MULTI-1D results in the target-normal direction and subsequently assess the possible influence of finite-focal-spot-induced transverse expansion.

For the underdense coronal region, the target-normal electron-density profile can be approximated by the one-dimensional isothermal self-similar expansion model [68],

$$n_e(s,t) = n_c \exp\left(-\frac{s}{c_s t}\right), \qquad s = x_c - x, \qquad c_s = \left(\frac{\bar{Z} k_{\mathrm{B}} T_e}{m_i}\right)^{1/2}, \tag{11}$$

where n_c is the critical electron density, x_c is the position of the critical-density surface, s denotes the target-normal distance measured from the critical-density surface toward the underdense side, c_s is the ion sound speed, $\bar{Z}$ is the average ionization state, and m_i is the ion mass. For the representative $\lambda_L = 1$ μm case at $t = 5$ ns, the MULTI-1D results in the $0.01n_c \le n_e \le 0.1n_c$ coronal region give $k_{\mathrm{B}}T_e \simeq 29.6$ eV and $\bar{Z} \simeq 2.99$, corresponding to $c_s \simeq 35.1$ μm/ns. The characteristic longitudinal density scale length extracted from the MULTI-1D profile is

$$L_n^{\mathrm{MULTI}} = \frac{|x_{0.01n_c} - x_{0.1n_c}|}{\ln 10} \simeq 185 \ \mu\mathrm{m}, \tag{12}$$

whereas the one-dimensional isothermal model gives

$$L_n^{\mathrm{theory}} = c_s t \simeq 176 \ \mu\mathrm{m}. \tag{13}$$

The difference is approximately 5%. As shown in Fig. 6, MULTI-1D and the one-dimensional self-similar model therefore predict comparable target-normal density-decay scales over the principal underdense coronal region. This agreement indicates that MULTI-1D provides a reasonable description of the characteristic target-normal coronal expansion under the representative conditions considered here. It should be emphasized, however, that this comparison assesses only the longitudinal consistency of the

one-dimensional treatment and does not imply that transverse expansion can be neglected for a finite laser focal spot.

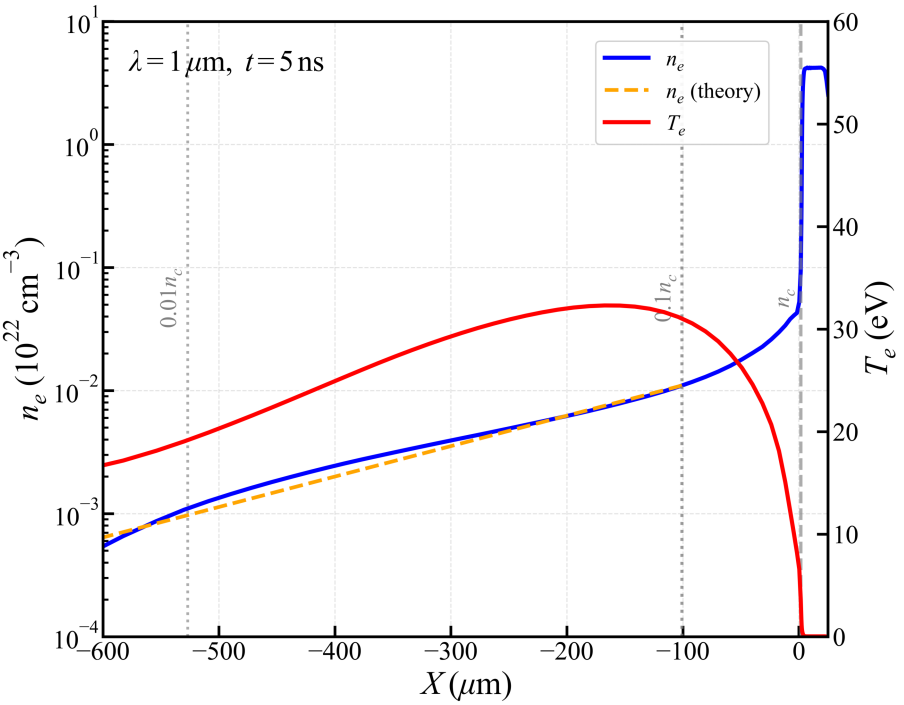


Fig. 6. Longitudinal electron-density and electron-temperature profiles from MULTI-1D for $\lambda_L = 1$ μm at $t = 5$ ns. The dashed curve denotes the electron-density profile predicted by the one-dimensional isothermal self-similar expansion model. The vertical dotted lines mark the $0.01n_c$, $0.1n_c$, and n_c density surfaces.

For a finite focal spot, transverse plasma expansion may become important. To qualitatively assess this multidimensional effect, we adopted the axisymmetric two-dimensional isothermal expansion model of Lan et al.[68]. In this model, the transition from one-dimensional to two-dimensional expansion is characterized by the $0.1n_c$, $0.01n_c$, and $0.001n_c$ density surfaces, with higher-density regions approaching the quasi-steady state earlier than lower-density regions. The analytical reconstruction uses the same representative Li-plasma parameters as in Fig. 6. The one-dimensional longitudinal density profiles were combined with the transverse profile of the two-dimensional quasi-steady solution while preserving the on-axis density. A representative focal-spot radius of $R_f = 60$ μm was used only to illustrate the finite-spot effect and is not an input parameter of the MULTI-1D calculations.

As shown in Fig. 7, finite-focal-spot-induced transverse expansion can produce substantial radial rarefaction, transforming the laterally uniform density distribution assumed in the one-dimensional planar treatment into a two-dimensional nonuniform structure. The associated redistribution of plasma density and temperature may modify the spatial extent and width of the EUV-emitting region. Transverse expansion may also alter the local energy density and EUV emissivity, while the accompanying density reduction may decrease the optical depth and radiation self-absorption. Consequently, multidimensional effects may influence the absolute CE through competing mechanisms. Their net quantitative contribution, however, cannot be determined from the present analytical density reconstruction alone and requires a self-consistent two- or three-dimensional radiation-hydrodynamic calculation.

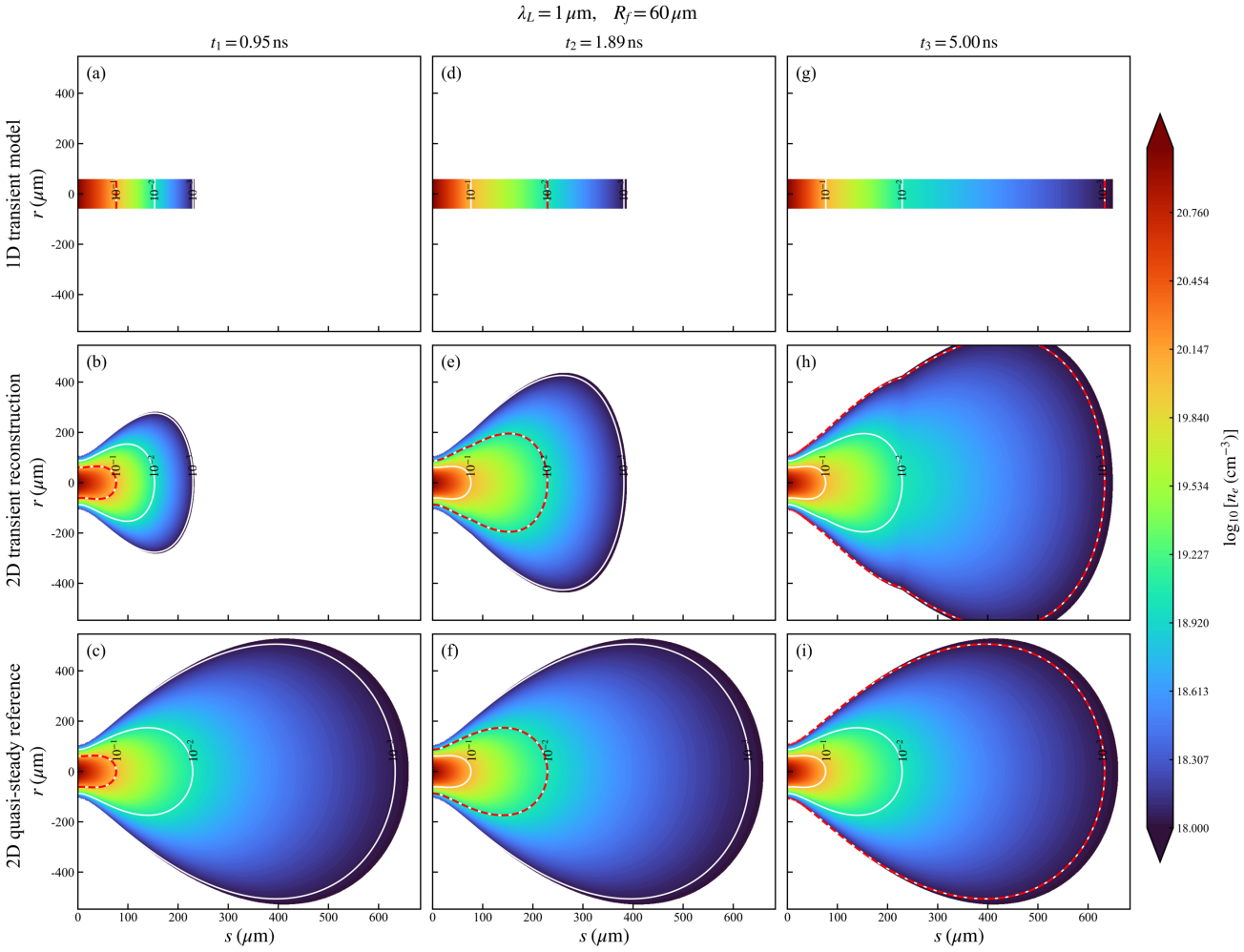


Fig. 7.

Analytical reconstruction of the transition from one-dimensional to two-dimensional plasma expansion for the representative $\lambda_L = 1\ \mu$m Li-plasma case with an illustrative focal-spot radius of $R_f = 60\ \mu$m. The three columns correspond to the characteristic stages associated with the $0.1n_c$, $0.01n_c$, and $0.001n_c$ density surfaces, respectively. Panels (a), (d), and (g) show the one-dimensional transient analytical distributions; panels (b), (e), and (h) show the reconstructed two-dimensional transient density distributions; and panels (c), (f), and (i) show the analytical two-dimensional quasi-steady reference distribution. The red dashed contour denotes the characteristic density surface associated with each stage.

4.2. Sensitivity to laser pulse profile and energy fluctuations

The baseline calculations assume a spatially uniform 10 ns square laser pulse. In practical high-energy harmonic laser systems, nonlinear harmonic conversion may introduce temporal-profile distortion, beam-quality degradation, and pulse-energy fluctuations. To evaluate the influence of realistic laser-pulse imperfections on the predicted EUV conversion efficiency, a sensitivity analysis was performed for the 0.266 μm, 0.35 μm, and 0.5 μm cases. Four laser-pulse conditions were considered: the original ideal 10 ns square pulse, a measured square-like 10 ns pulse [69], and ideal square pulses with -2.5% and $+2.5\%$ variations in pulse energy, as shown in Fig. 8. The $\pm 2.5\%$ range was chosen as a conservative sensitivity interval based on the reported energy stability of high-energy harmonic laser systems [70].

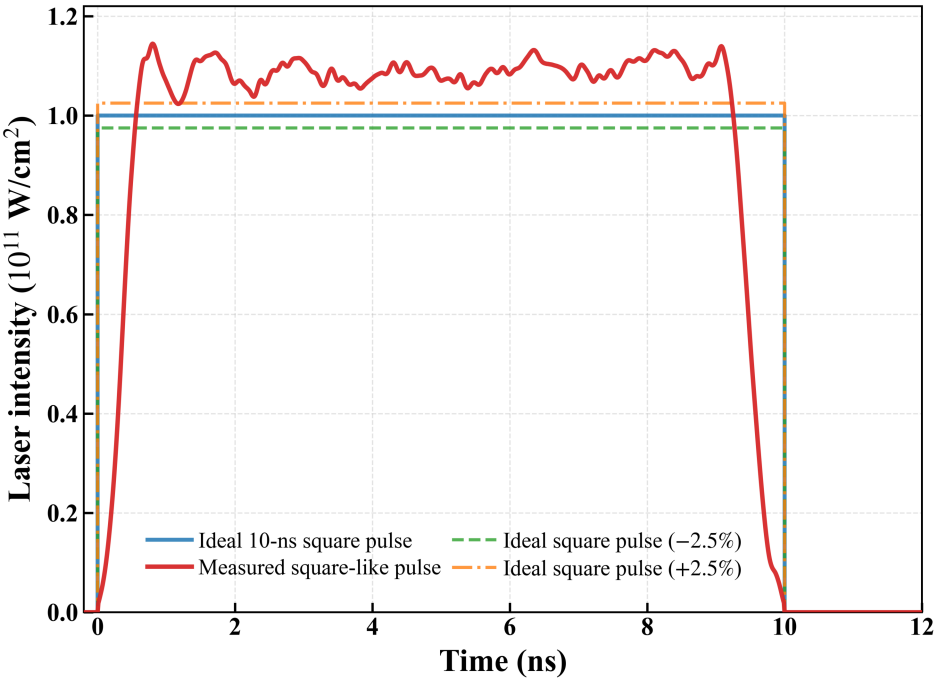


Fig. 8. Laser pulse conditions considered in the sensitivity analysis: ideal 10 ns square pulse, measured square-like 10 ns pulse, and ideal square pulses with −2.5% and +2.5% variations in pulse energy. The same four conditions were applied to the 0.266 μm, 0.35 μm, and 0.5 μm cases.

As shown in Table 1, the predicted CE remains nearly unchanged under all tested temporal-profile and pulse-energy variations. At 0.266 μm, the CE values range only from 2.39% to 2.43%; at 0.35 μm, from 2.41% to 2.46%; and at 0.5 μm, from 2.49% to 2.54%. In each case, the spread across the ideal square pulse, measured square-like pulse, and ±2.5% pulse-energy conditions is no more than 0.05 percentage points. These results demonstrate that the predicted CE is robust against the experimentally relevant temporal-profile and pulse-energy variations considered here.

Table 1. Calculated CE at 0.266 μm, 0.35 μm, and 0.5 μm under the four laser pulse conditions used in the sensitivity analysis.

Laser temporal profile	CE (0.266 μm)	CE (0.35 μm)	CE (0.5 μm)
Ideal 10-ns square pulse	2.39%	2.44%	2.50%
Measured square-like profile	2.43%	2.46%	2.54%
Ideal square pulse (−2.5%)	2.39%	2.41%	2.49%
Ideal square pulse (+2.5%)	2.40%	2.45%	2.51%

4.3. Surrogate-model selection and statistical robustness of Bayesian optimization

To examine the influence of the surrogate model and the stochastic nature of BO on the optimization performance, ten independent optimization runs with different random seeds were performed under identical optimization settings and the same budget of 50 objective-function evaluations. In addition to the RF surrogate, an NN-based surrogate was implemented within the BO framework as an additional

nonlinear model, while a GPR surrogate was also considered for comparison. The three surrogate models were evaluated using the same five-point LHS initialization, discrete parameter space, dynamic UCB acquisition strategy, and objective function.

The statistical results are summarized in Table 2. The RF-based BO identified the reference global optimum in 8 out of 10 independent runs, corresponding to an 80% success rate. In comparison, the NN-based and GPR-based BO methods achieved success rates of 50% and 0%, respectively. Among the successful runs, the RF- and NN-based BO methods required 31.6 ± 6.9 and 33.2 ± 7.3 objective-function evaluations, respectively, to identify the reference global optimum, where the uncertainties represent the standard deviations across the successful runs. When all ten independent runs are considered, the final best CE values are $2.44 \pm 0.13\%$, $2.39 \pm 0.16\%$, and $2.21 \pm 0.18\%$ for the RF-, NN-, and GPR-based BO methods, respectively. These results demonstrate that the RF-based BO achieves the highest success rate while maintaining a relatively small variation in the optimization results, indicating more robust and stable performance for the present optimization problem.

Table 2. Performance of different Bayesian optimization surrogate models

Method	Runs	Success rate	Evaluations to global optimum	Final best CE (%)
BO (RF)	10	8/10 (80%)	31.6 ± 6.9	2.44 ± 0.13
BO (NN)	10	5/10 (50%)	33.2 ± 7.3	2.39 ± 0.16
BO (GPR)	10	0/10 (0%)	N/A	2.21 ± 0.18

5. Conclusion

This work investigates the EUV emission characteristics of short-wavelength solid-state laser-driven Li plasmas and performs rapid global optimization of the EUV CE using an improved Bayesian optimization framework. The highest in-band CE within a 2% bandwidth centered at 13.5 nm reaches 2.5% at a laser wavelength of 0.5 μm and a laser intensity of 6×10^{10} W/cm^2, while maintaining a relatively high SP of 22.4%. In addition, the optimal laser intensity is found to decrease with increasing wavelength, following the scaling law $I_{L,\mathrm{peak}} \propto \lambda_L^{-1.9}$. More importantly, the present study reveals that the evolution of the CE is governed by the competition between radiation enhancement and spectral broadening effects. Shorter-wavelength lasers increase the critical density and strengthen local energy deposition in high-density plasma regions, thereby improving the radiation efficiency. However, the resulting increase in plasma optical depth enhances radiation self-absorption and re-emission processes, leading to spectral broadening and degradation of the SP. The balance between these competing mechanisms ultimately determines the achievable CE under different laser conditions.

The one-dimensional simulations also reproduce the main CE–intensity trends and major spectral features observed in reported Li-target experiments. Nevertheless, finite-spot lateral expansion and trans-

verse radiation transport are not included in the present planar model and may affect the absolute CE. Furthermore, by combining Latin hypercube sampling, a dynamically adjusted acquisition function, and a random-forest surrogate, the improved Bayesian optimization strategy identifies the global optimum in a representative run after only 25 total objective-function evaluations, compared with 272 simulations required for exhaustive grid search. The present results demonstrate the potential of Bayesian optimization for efficient parameter optimization within the current two-variable discrete parameter space. Extension to additional laser and target parameters and multidimensional radiation-hydrodynamic simulations remains a subject for future work.

Appendix A: Benchmark of the MULTI-1D model against Li-target experiments

To further assess the quantitative reliability of the present radiation-hydrodynamic model, additional benchmark calculations were performed against available experimental data for laser-produced Li plasmas. These calculations were carried out separately from the parameter scans discussed in the main text, with the simulation conditions adjusted to reproduce the corresponding experimental conditions as closely as possible. Two complementary comparisons are presented below: the CE–intensity dependence measured by Nagano et al. [37] and the time-integrated EUV spectrum reported by George et al. [71].

First, the calculated CE–intensity dependences were benchmarked against the planar Li-target measurements. For this comparison, additional simulations were performed under conditions closely matching the experiment, using a 380 μm-thick planar Li target, a 10-ns laser pulse, and laser wavelengths of 1064 and 532 nm. As shown in Fig. A1, the simulations reproduce the overall magnitude of the measured CE and the general trend that the optimum laser intensity shifts toward higher values and the maximum CE increases as the laser wavelength decreases from 1064 to 532 nm. However, the calculated CE–intensity curves are steeper than the experimental data, and the calculated optimum intensity for the 1064-nm case is greater than the experimental value. At 532 nm, the laser intensity at which the maximum CE is obtained is in good agreement with the experiment. These differences are likely associated mainly with finite-focal-spot and multidimensional plasma effects [72].

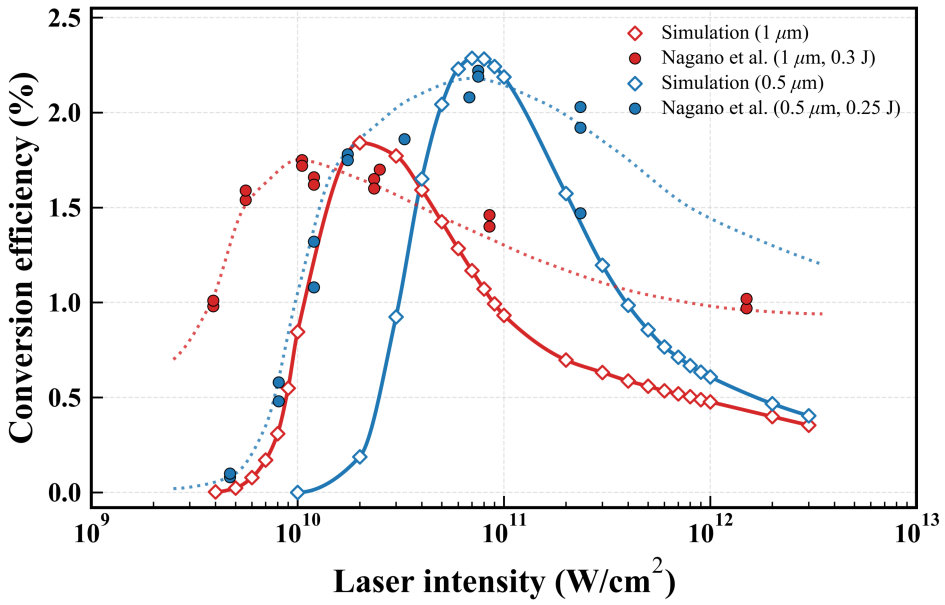


Fig. A1. Comparison of the calculated CE–intensity dependences with the experimental Li-target results at 1064 and 532 nm.

Second, the calculated time-integrated EUV spectrum at 1064 nm was compared with the experimental Li spectrum. The photon-energy grid in the simulation was refined to 136 groups over the photon-energy range of 1–400 eV to improve the representation of the narrow Li emission features. As shown in Fig. A2, the dominant 13.5-nm feature and the major spectral structures near approximately 10.8, 11.4, 17.8, and 19.9 nm are reproduced in the corresponding wavelength regions. Some narrow experimental features are broadened because of the finite multigroup spectral resolution.

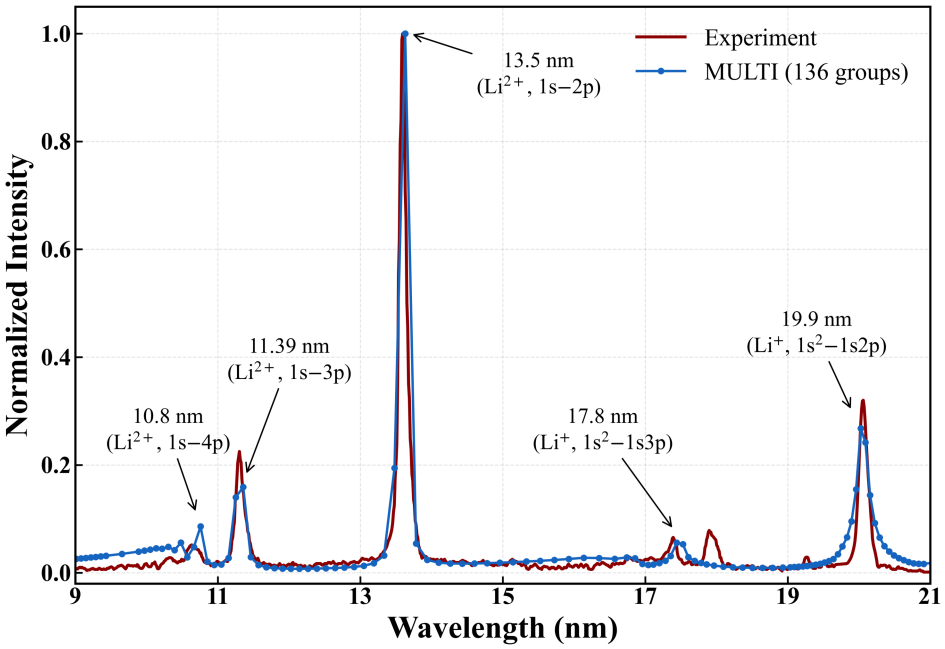


Fig. A2. Comparison of the calculated time-integrated EUV spectrum with the experimental Li spectrum at 1064 nm.

To quantify the agreement in the overall spectral-energy distribution, both spectra were integrated over the same 9–21 nm wavelength range. The spectral distribution was further divided into three broad

wavelength intervals, as summarized in Table A1. The experimental and calculated fractions are 23.03% and 23.71% for 9–13 nm, 49.64% and 50.09% for 13–17 nm, and 27.33% and 26.20% for 17–21 nm, respectively. The maximum difference among the three spectral regions is only 1.13 percentage points. These results indicate good agreement in the overall spectral-energy distribution.

Table A1. Quantitative comparison of the integrated spectral distribution between the MULTI-1D calculation and experiment.

Spectral range	Experiment (%)	MULTI-1D (%)	Difference (pp)*
9–13 nm	23.03	23.71	−0.68
13–17 nm	49.64	50.09	−0.45
17–21 nm	27.33	26.20	+1.13

*Difference is defined as the experimental result minus the simulation result, and pp denotes percentage points.

Overall, the agreement in the CE–intensity dependence, the major spectral features, and the integrated spectral-energy distribution provides quantitative support for the reliability of the present MULTI-1D calculations. The remaining discrepancies are consistent with the finite multigroup spectral resolution and the limitations of the one-dimensional planar approximation.

Acknowledgment

Project supported by the National Natural Science Foundation of China (Grant No. 12305270), the High-level Talent Program of University of South China (Grant No. 5524GC015), the Strategic Priority Research Program of the Chinese Academy of Sciences (Grant No. XDA0380000) and Natural Science Foundation of Shanghai (Grant No. 25JD1404100).

References

[1] Torretti F, Sheil J, Schupp R, Basko M M, Bayraktar M, Meijer R A, Witte S, Ubachs W, Hoekstra R, Versolato O O, Neukirch A J and Colgan J 2020 *Nat. Commun.* **11** 2334

[2] Behnke L, Schupp R, Bouza Z, Bayraktar M, Mazzotta Z, Meijer R, Sheil J, Witte S, Ubachs W, Hoekstra R and Versolato O O 2021 *Opt. Express* **29** 4475

[3] Min Q, Wang G D, He C W, He S Q, Lu H D, Liu X B, Wu Y H, Su M G and Dong C Z 2025 *Acta Phys. Sin.* **74** 033201 (in Chinese)

[4] Miao W W, He H Y, Tao Y, Wu Q, Wu C and Liu C H 2025 *Chin. Phys. B* **34** 106501

[5] Lin N, Yang W H, Chen Y Y, Wei X, Wang C, Zhao J L, Peng Y J and Leng Y X 2022 *Laser Optoelectron. Prog.* **59** 0922002 (in Chinese)

[6] Wen Z L, Xie Z, Wang C H, Zhang Q J, Song X W, Dou Y P, Li B C, Pan Q K, Chen F, Zhao C X and Lin J Q 2024 *Opt. Express* **32** 37779

[7] Lyu T H, Song Y J, Zong N, Zhang S J, Bo Y and Peng Q J 2025 *Laser Technol.* **49** 328 (in Chinese)

[8] Zhang X H, Wang W H, He C N, Yao Y C, Wang B Y, Li X H, Wang Z J, Qiu C, Sun H Y, Leng Y X and Xin G 2025 *Chin. Phys. B* **34** 114701

[9] Ren C, Yuan Y, Sun W and Wang Z 2025 *Plasma Sources Sci. Technol.* **34** 055001

[10] Min Q, He C W, Lu H D, Liu X B, Su M G and Dong C Z 2025 *Phys. Rev. Res.* **7** 043155

[11] He C W, Min Q, He S Q, Li H Y, Lu H D and Su M G 2026 *Phys. Plasmas* **33** 012103

[12] Han X, Fu Y Y 2026 *Plasma Sci. Technol.* **28** 045001

[13] Zong N, Hu W M, Wang Z M, Wang X J, Zhang S J, Bo Y, Peng Q J and Xu Z Y 2020 *Chin. Opt.* **13** 28 (in Chinese)

[14] Ji L L, Wang W T, Tian Y, et al. 2024 *Chin. J. Lasers* **51** 1101003 (in Chinese)

[15] Schupp R, Torretti F, Meijer R A, Bayraktar M, Scheers J, Kurilovich D, Bayerle A, Eikema K S E, Witte S, Ubachs W, Hoekstra R and Versolato O O 2019 *Phys. Rev. Appl.* **12** 014010

[16] Basko M M 2016 *Phys. Plasmas* **23** 083114

[17] Hu Z L, Wang T Z, He L, Lin N, Leng Y X and Chen W B 2025 *Spectrosc. Spectral Anal.* **45** 1834 (in Chinese)

[18] Tanaka H, Matsumoto A, Akinaga K, Takahashi A and Okada T 2005 *Appl. Phys. Lett.* **87** 041503

[19] Kim J, Lee B, Matsuo K, Bailly-Grandvaux M and Beg F N 2025 *J. Appl. Phys.* **138** 033109

[20] Ren C, Yuan Y, Sun W, Lv C and Wang Z 2025 *Phys. Plasmas* **32** 103501

[21] Hu Z L, He L, Wang T Z, Lin N and Leng Y X 2025 *Chin. J. Lasers* **52** 0601001 (in Chinese)

[22] Shimada Y, Nishimura H, Nakai M, Hashimoto K, Yamaura M, Tao Y, Shigemori K, Okuno T, Nishihara K, Kawamura T, Sunahara A, Nishikawa T, Sasaki A, Nagai K, Norimatsu T, Fujioka S, Uchida S, Miyanaga N, Izawa Y and Yamanaka C 2005 *Appl. Phys. Lett.* **86** 051501

[23] Tao Y, Ueno Y, Yuspeh S, Burdt R, Tillack M S and Najmabadi F 2011 *Proc. SPIE* **7969** 796930

[24] Mostafa Y, Behnke L, Engels D J, Bouza Z, Sheil J, Ubachs W and Versolato O O 2023 *Appl. Phys. Lett.* **123** 234101

[25] Hemminga D J, Versolato O O and Sheil J 2023 *Phys. Plasmas* **30** 033301

[26] Shi Z Y, Yuan Y, Wang W P, Ma Y Y, Sun X Y, Lin N and Leng Y X 2023 *Phys. Plasmas* **30** 043107

[27] Ma H T, Yuan Y, Shi Z Y, Xie X Y, Wang M J, Wang W P, Ding C Y, Leng Y X and Li R X 2025 *AIP Adv.* **15** 055304

[28] Dong Y L, Xu B H, Yang X H, Wu Y T, Xiong W, Zhang G B and Ma Y Y 2025 *Opt. Express* **33** 43894

[29] Dong Y L, Xu B H, Xiong W, Yang X H, Ma H H, Zhang G B, Wu Y T and Ma Y Y 2025 *Phys. Plasmas* **32** 123301

[30] Schupp R, Behnke L, Bouza Z, Mazzotta Z, Mostafa Y, Lassise A, Poirier L, Sheil J, Bayraktar M, Ubachs W, Hoekstra R and Versolato O O 2021 *J. Phys. D: Appl. Phys.* **54** 365103

[31] Coons R W, Harilal S S, Campos D and Hassanein A 2010 *J. Appl. Phys.* **108** 063306

[32] Mojarad N, Gobrecht J and Ekinci Y 2015 *Sci. Rep.* **5** 9235

[33] Dou Y P, Xie Z, Song X L, Tian Y and Lin J Q 2015 *Acta Phys. Sin.* **64** 235202 (in Chinese)

[34] Xie Z, Wen Z L, Si M Q, Dou Y P, Song X W and Lin J Q 2022 *Acta Phys. Sin.* **71** 035202 (in Chinese)

[35] Schriever G, Bergmann K and Lebert R 1998 *J. Appl. Phys.* **83** 4566

[36] Nica P E, Miyamoto S, Amano S, Inoue T, Shimoura A, Kaku K and Mochizuki T 2006 *Appl. Phys. Lett.* **89** 041501

[37] Nagano A, Mochizuki T, Miyamoto S and Amano S 2008 *Appl. Phys. Lett.* **93** 091502

[38] Coons R W, Harilal S S, Polek M and Hassanein A 2011 *Anal. Bioanal. Chem.* **400** 3239

[39] Higashiguchi T, Kawasaki K, Senba Y, Suetake S, Katto M and Kubodera S 2007 *Proc. SPIE* **6346** 63462R

[40] Ramis R, Schmalz R and Meyer-ter-Vehn J 1988 *Comput. Phys. Commun.* **49** 475

[41] Ramis R, Eidmann K, Meyer-ter-Vehn J and Hüller S 2012 *Comput. Phys. Commun.* **183** 637

[42] Ramis R and Meyer-ter-Vehn J 2016 *Comput. Phys. Commun.* **203** 226

[43] Turnbull D, Katz J, Sherlock M, Divol L, Shaffer N R, Strozzi D J, Colaïtis A, Edgell D H, Follett R K, McMillen K R, Michel P, Milder A L and Froula D H 2023 *Phys. Rev. Lett.* **130** 145103

[44] Ashcroft N W and Mermin N D 1976 *Solid State Physics* (New York: Harcourt College Publishers)

[45] Chung H K, Chen M H, Morgan W L, Ralchenko Y and Lee R W 2005 *High Energy Density Phys.* **1** 3

[46] More R M, Warren K H, Young D A and Zimmerman G B 1988 *Phys. Fluids* **31** 3059

[47] Hansson B A M, Fomenkov I V, Böwering N R, Ershov A I, Partlo W N, Myers D W, Khodykin O V, Bykanov A N, Rettig C L, Hoffman J R, Vargas L E, Simmons R D, Chavez J A, Marx W F and Brandt D C 2006 *Proc. SPIE* **6151** 61510R

[48] Basko M M, Novikov V G, Grushin A S 2015 *Phys. Plasmas* **22** 053111

[49] Yuan Y, Ma Y Y, Wang W P, Chen S J, Cui Y, Zi M, Yang X H, Zhang G B and Leng Y X 2022 *Plasma Phys. Control. Fusion* **64** 025001

[50] Miyamoto S, Amano S, Inoue T, Nica P E, Shimoura A, Kaku K, Sekioka T and Mochizuki T 2006 *Proc. SPIE* **6151** 61513S

[51] Li M, Zhang H P, Chen S, Tao P D, Zhu H, Zhou C T, Zhao J H and Sun C W 2022 *High Power Laser Part. Beams* **34** 011001 (in Chinese)

[52] Atzeni S and Meyer-ter-Vehn J 2008 *The Physics of Inertial Fusion* (Beijing: Science Press) pp. 186–190 (in Chinese)

[53] Versolato O O 2019 *Plasma Sources Sci. Technol.* **28** 083001

[54] Wang T Z, Hu Z L, He L, Lin N, Leng Y X and Chen W B 2025 *Vacuum* **231** 113805

[55] Wen Z L, Xie Z, Wang C H, Zhang Q J, Si M Q, Song X W, Dou Y P, Li B C and Lin J Q 2024 *Vacuum* **224** 113145

[56] Nishihara K, Sunahara A, Sasaki A et al. 2008 *Phys. Plasmas* **15** 056708

[57] Hoffman J R, Bykanov A N, Khodykin O V, Ershov A I, Böwering N R, Fomenkov I V, Partlo W N and Myers D W 2005 *Proc. SPIE* **5751** 892

[58] Wu T, Wu T, Zhou S C, Liao Q, Lu P X 2025 *Plasma Sci. Technol.* **27** 075501

[59] Djordjevic B Z, Kemp A J, Kim J, Simpson R, Wilks S C, Ma T and Mariscal D 2021 *Phys. Plasmas* **28** 043105

[60] Jalas S, Kirchen M, Messner P, Winkler P, Hübner L, Dirkwinkel J, Schnepp M, Lehe R and Maier A R 2021 *Phys. Rev. Lett.* **126** 104801

[61] Dolier E J, King M, Wilson R, Gray R J and McKenna P 2022 *New J. Phys.* **24** 073025

[62] Loughran B, Streeter M J V, Ahmed H et al. 2023 *High Power Laser Sci. Eng.* **11** e35

[63] Wang X L, Jin Y C, Schmitt S and Olhofer M 2023 *ACM Comput. Surv.* **55** 287

[64] Shields M D and Zhang J X 2016 *Reliab. Eng. Syst. Saf.* **148** 96

[65] Zhang W G, Wu C Z, Zhong H Y, Li Y Q and Wang L 2021 *Geosci. Front.* **12** 469

[66] Hutter F, Hoos H H and Leyton-Brown K 2011 *Proc. LION 5* p. 507

[67] Dahmani F 1993 *J. Appl. Phys.* **74** 622

[68] Lan X, Li X C, Yang S Y, Tang H B, Kuang L Y and Hu G Y 2025 *High Power Laser Part. Beams* **37** 052003 (in Chinese)

[69] Meijer R, Stodólna A, Eikema K and Witte S 2017 *Opt. Lett.* **42** 2758

[70] Li J T, Zhang J Y, Ma T J, Yao Y P, Liang R Z, Zhou X, Jia C Y, Huang S J, Nie H K, Yao B, He J L and Zhang B T 2024 *High Power Laser Sci. Eng.* **12** e68

[71] George S A, Silfvast W, Takenoshita K, Bernath R, Koay C S, Shimkaveg G, Richardson M, Al-Rabban M and Scott H 2006 *Proc. SPIE* **6151** 615143

[72] Fujioka S, Nishimura H, Nishihara K, Sasaki A, Sunahara A, Okuno T, Ueda N, Ando T, Tao Y Z, Shimada Y, Hashimoto K, Yamaura M, Shigemori K, Nakai M, Nagai K, Norimatsu T, Nishikawa T, Miyanaga N, Izawa Y and Mima K 2005 *Phys. Rev. Lett.* **95** 235004